ANNUAL REPORT

for NASA grant NAGW 3543 titled

SeaWiFS CALIBRATION AND ALGORITHM VALIDATION

Submitted by:

Robert J. Parada, Jr.
Graduate Student

Philip N. Slater
Principal Investigator

Remote Sensing Group
Optical Sciences Center
University of Arizona
Tucson, Arizona 85721

October 1996

Table of Contents

INTRODUCTION AND SUMMARY

This is the fourth annual report on NASA grant NAGW 3543, titled "SeaWiFS Calibration and Algorithm Validation" covering the period from November 1, 1995 to October 31, 1996. The work discussed herein, unless otherwise noted, was completed primarily by R. Parada with the assistance of K. Thome, and R. Santer. R. Parada is a graduate student in the Remote Sensing Group (RSG); K. Thome is an assistant professor in Optical Sciences at the University of Arizona and R. Santer is a professor of Atmospheric Optics at the University of Littoral, France.

An extended field experiment was conducted at Lake Tahoe in late July 1996. Personal involved in this effort include R. Parada, K. Thome, J. LaMarr, E. Nelson, and C. Curtis. There were several goals for the trip: 1) experimental verification of radiative transfer computations for various viewing geometries; 2) retrieval of an effective aerosol optical depth scale height; 3) calibration of a large field of view (FOV) sensor; 4) evaluation of spatial non-uniformities in surface reflectance. To accomplish the first goal, aircraft-based measurements were collected at a variety of viewing angles over the lake. The field radiometer used was positioned using a custom mount developed specifically for the research. Altitudes typically flown during calibrations conducted over the lake were employed for this work. To evaluate the ability to retrieve an effective aerosol optical depth scale height, which is a source of uncertainty primarily for the radiance-based calibration method, measurements of upwelled radiance were made at several altitudes over the lake with a vertically mounted airborne radiometer. The application of the reflectance- and radiance-based methods of calibration to a large FOV sensor was attempted during an overpass of AVHRR-14. Finally, both in-water samples and aircraft-based photographs were collected to help evaluate and determine the reasons for the persistence of non-uniform reflectance areas on the lake. The majority of these data have yet to be reduced and will figure prominently in the efforts of the group during the next few months.

The investigation and development of novel methods for the calibration of field radiometers at a variety of signal levels has been continued during the past year. The radiometer flown during the June 1995 campaign at Lake Tahoe is being characterized using four separate methods: 1) lamp standard-based calibration; 2) solar radiation-based calibration; 3) molecular scatter-based calibration; and 4) spherical integrating source-based calibration. The intercomparison of these techniques should help determine the existence of any biases in them. The range of radiance levels provided will also allow the determination of linearity in the calibrations. While methods (1) and (4) must be conducted in a laboratory environment, the remaining two techniques offer the possibility of calibrating radiometers in the field. This investigation should be completed by early November 1996.

During the June 1995 Lake Tahoe campaign, regions having non-uniform reflectances were discovered. Modeling work has been conducted to try to ascertain the reason for this effect. This work, completed by M. Chami of the University of Littoral, made use of AVIRIS imagery collected during the June campaign. The modeling work was carried out using both the Successive Orders software (which is used during the vicarious calibration

process) and the HYDROLIGHT 3.0 radiative transfer code developed by C. Mobley. These tools have provided leads for the source of the phenomenon. It is hoped that the in-water samples collected during the July 1996 field trip, when analyzed, will confirm the modeling results.

Much of the work accomplished this past year has built on the work done during the June 1995 field campaign to Lake Tahoe. The calibration data resulting from this trip have been analyzed and a preliminary set of uncertainties have been assigned to the vicarious methods used. These uncertainties have helped to refine the research to areas which introduce the largest unknowns into the calibration processes. A paper submitted to the SPIE EUROPTO 1996 conference in Italy this past September which details this work has been included with this report.

A second paper, also included with this report, details the results of numerical fitting of wave-slope models. This work has improved the accuracy of radiative transfer computations conducted for a rough water target, like Lake Tahoe.

In the months to come, the reduction of the data collected during the July 1996 campaign will take precedence. In addition, the measured water properties will be used to better model surface non-uniformities at Lake Tahoe. Finally, attention will be turned to the improvement of the field radiometer and mount used during the radiance-based calibration process.

Results of dark target vicarious calibration using Lake Tahoe

R. J. Parada, K. J. Thome, and R. P. Santer*

Remote Sensing Group (RSG), Optical Sciences Center, University of Arizona
Tucson, Arizona 85721

*Laboratoire de Physique Appliquée au Milieu Océanique Côtier - Station Marine,
Université du Littoral, 62930 Wimereux, France

ABSTRACT

The ability to conduct in-flight absolute radiometric calibrations of ocean color sensors will determine their usefulness in the decade to come. On-board calibration systems are often integrated into the overall system design of such sensors and have claimed uncertainty levels from 2-3%, but independent means of system calibration are desirable to confirm that such systems are operating properly.[1] Vicarious methods are an attractive means of this verification. Due to the high sensitivity of ocean color sensors, the use of bright reflectance surfaces often results in sensor saturation. Low reflectance targets, such as water bodies, should therefore be used. This paper presents the results of sensitivity studies of the reflectance- and radiance-based approaches when applied to a water target and method uncertainties for calibrations of the Sea-Viewing Wide Field-of-view Sensor (SeaWiFS). The paper also presents the results of a field campaign which took place at Lake Tahoe in June 1995. This lake represents a typical oligotrophic water body and has the advantage of being located at a high elevation where tropospheric aerosol loading is low. Aircraft-based radiance data and surface measurements of reflectance are used to calibrate SeaWiFS-simulated bands from Advanced Visible and InfraRed Imaging Spectrometer (AVIRIS) data. Atmospheric characterization is obtained using solar extinction measurements, surface-level atmospheric pressure readings, and columnar gaseous absorber amounts at sensor overpass. The measured radiances are transferred to the top of the atmosphere (TOA) using a radiative transfer code which fully computes the contributions of multiple scattering by the atmosphere. The results are compared to those obtained from a laboratory-based calibration of AVIRIS.

1. INTRODUCTION

1.1. History of vicarious calibration

In-flight, absolute radiometric calibrations of sensors are necessary to insure that the data they acquire are quantitatively useful. On-board calibration systems are often integrated into the overall system design of such sensors. These systems sometimes do not perform complete end-to-end calibrations[2] and tend to degrade over time[3-4]. Independent means of calibration, like vicarious methods, are therefore needed to verify the calibration results from such systems.

Vicarious sensor calibration techniques have been used by the RSG for over ten years. With these methods, sensors such as the Landsat Thematic Mapper (TM) and the Système Pour l'Observation de la Terre Haute Resolution Visible (SPOT HRV) have been successfully calibrated on numerous occasions.[2-3,5] These instruments have spectral bands covering the visible portion of the spectrum, have been designed to view terrestrial targets, and tend to have nadir footprints on the order of 100-400 m^2. These features make vicarious calibration well-suited for the sensors. Desertic sites like White Sands Missile Range (WSMR), New Mexico and areas in the Sahara have been used as calibration targets for such sensors.[2-3,6] These sites have bright, spectrally flat reflectances that are spatially and temporally uniform and have low aerosol loading.

1.2. Ocean color sensors

Like many terrestrial viewing sensors, ocean color sensors typically cover the visible and near-infrared portions of the electromagnetic spectrum.[7-8] However, few other design features are similar between these two sensor varieties. Ocean color sensors tend to have low spatial resolutions - typically on the order of 1 km^2 to allow daily coverage of the Earth's oceans. These sensors have high signal sensitivities to retrieve in-water reflectances and determine quantities such as chlorophyll concentration and sediment content. This prohibits the use of desertic

calibration sites since the sensors saturate from the signal levels upwelled by such targets. Low reflectance targets with a high degree of spatial and (hopefully) temporal uniformity are needed for vicarious calibration targets.

Using low reflectance targets, however, adds a number of complexities to the problem of vicarious calibration. These result largely from the fact that the atmosphere contributes a much higher portion of the radiance signal present at sensor level. In order to achieve the same calibration uncertainty levels, the atmospheric characterization must be better than is necessary when using high reflectance targets. More subtle differences also exist for the calibration of ocean color sensors. These sensors typically view Case I waters, which have highly directional reflectance properties. The problem of properly modeling the radiative transfer process is therefore different than for (nearly lambertian) land sites. As a result, it is preferable to conduct vicarious calibrations of ocean color sensors over water targets so that the operational conditions of the sensors are more closely reproduced.

1.3. Site selection and nominal conditions for the calibration of SeaWiFS

The RSG is responsible for the in-flight vicarious calibration of SeaWiFS. Lake Tahoe has been selected as a possible low-reflectance target for this work. This is a deep volcanic lake containing clear, oligotrophic water that is located at an elevation of approximately 1.9 km above mean sea level (MSL). The local aerosol loading is low and the particles are continental in nature.

A summary of representative environmental conditions for Lake Tahoe is presented in Table 1. These data were acquired during a field campaign to Lake Tahoe in June 1995. The listed parameters correspond to spectral inputs of the radiative transfer code used during the vicarious calibration process. Additional parameters for this site include the real aerosol index $n_{aerosol}=1.44$, the imaginary aerosol index $k_{aerosol}=-0.005$, the single scattering albedo $\omega_o=0.859$, and the aerosol Ångstrom turbidity coefficient $\nu=1.08$.

Table 1. Nominal Lake Tahoe environmental conditions for the eight SeaWiFS bands.

Band	Center Wavelength (μm)	Aerosol Optical Depth, $\delta_{aerosol}$	Molecular Optical Depth, $\delta_{molecular}$	In-Water Diffuse Reflectance, ρ_{water}
1	0.412	0.080	0.255	0.018
2	0.443	0.075	0.190	0.018
3	0.490	0.063	0.126	0.018
4	0.510	0.056	0.106	0.014
5	0.555	0.051	0.075	0.008
6	0.670	0.037	0.035	0.001
7	0.765	0.035	0.021	< 0.001
8	0.865	0.027	0.013	< 0.001

2. REFLECTANCE-BASED CALIBRATION

A number of sensors have been successfully calibrated by the RSG using the reflectance-based technique. The method has also been used by the Laboratoire d'Optique Atmosphérique (LOA) of the University of Lille, France.[9] The technique uses measurements of reflectance over a calibration site at sensor overpass. Optical extinction measurements and meteorological data are used to retrieve spectral optical depths and gaseous absorption constituents. These parameters are used to characterize the effect of the atmosphere on the TOA radiance field via a suitable radiative transfer code. The ratio of the computed radiance to the digital number (DN) recorded by the sensor becomes the absolute radiometric calibration coefficient for a given sensor band. Exoatmospheric solar irradiance is therefore the source for this method.

2.1. Radiative transfer code

The radiative transfer code selected for use with vicarious calibrations over water targets was the Successive Orders[10] (SO) program developed by the LOA. This code computes radiance contributions from multiple scattering. The radiative transfer equation for the upwelled radiance field is numerically solved for an atmosphere composed of molecules and spherical particles. This transfer equation is decomposed into a Fourier series as a function of azimuth for each of 24 view zenith angles (VZAs). Each VZA has an associated transfer equation which is solved separately. The model divides a plane-parallel, horizontally-homogeneous atmosphere into 26 layers of equal optical depth. Successive orders of scattering are introduced until the resulting radiance field converges or until the maximum scattering order (200) is reached. The primary advantage of using the SO transfer code is its ability to handle a rough ocean surface (i.e. one containing a random distribution of wave-slopes) and polarization, which affects the radiance field at the 4% level in the short wave visible region. Gaseous absorption is computed separately using the Simulation of the Satellite Signal in the Solar Spectrum (5S)[11] transfer code developed by the LOA. Band integrated transmittance values for ozone and water vapor are computed using columnar measurements while absorption from oxygen and other molecular gases are computed using standard atmospheric models.

For the reflectance-based method, the radiative transfer codes play a very important role. Atmospheric parameters measured during sensor overpass, along with the solar-sensor geometry, are used as code inputs. The incident exoatmospheric irradiance is transferred down through the modeled atmosphere and back up in the direction of sensor observation. This double-pass through the entire atmosphere results in a high-degree of sensitivity to the input parameters. Uncertainties in these parameters lead to uncertainties in the TOA radiances. For low reflectance targets, these uncertainties are higher due to the relative importance of atmospheric signal contributions.

2.2. Sensitivity study

In order to determine which parameters need to be best characterized to minimize vicarious calibration uncertainties, a general sensitivity study of the TOA radiances was conducted for all eight SeaWiFS bands.[8] The associated band centers are listed in Table 1. The environmental parameters presented in Section 1.3 were used as the nominal inputs for the associated transfer code trials. Solar zenith angles of approximately 20°, 40°, and 60° were selected. These angles span the range of solar conditions throughout the year at Lake Tahoe near local noon (i.e. the approximate time of SeaWiFS overpass). In addition, wind speeds of 0.0 m/s, 5.0 m/s, and 10.0 m/s were employed. These values span the range of conditions under which most calibrations will be attempted. The majority of the figures presented herein were created for the following conditions: a solar zenith angle near 20°; a near-nadir viewing geometry; a wind speed of 5.0 m/s; and SeaWiFS bands 1, 5, and 8. Percent changes, when presented, have been computed relative to the nominal input results.

Principal plane slices of the TOA apparent reflectance field, which is linearly related to the radiance field, over Lake Tahoe are presented in Figure 1. Note the characteristic peak in the specular or "sun glint" direction. This is also the direction of forward scatter. The radiance field becomes more concentrated about this direction at longer wavelengths for two reasons: 1) the optical depth is decreased so that the coupling of specularly reflected or "glint" radiances into other directions is reduced; 2) the radiance contribution from in-water reflectance is lower due to heightened absorption.

The major sources of uncertainty for the reflectance-based method may be subdivided into six categories: 1) choice of aerosol complex refractive index; 2) choice of aerosol size distribution; 3) measurement of optical depth; 4) computation of gaseous absorption; 5) aerosol vertical distribution; and 6) measurement of surface reflectance. Each category was investigated for the current work.

The RSG does not directly measure the aerosol complex refractive index. A representative value is selected based on recommendations of others in the field.[12] For the southwestern United States a standard value is 1.44 - 0.005i, though one of the authors has seen values ranging from 1.30 to 1.50 for the real index and from -0.01 to 0.00 for the imaginary index. Using this range of values as a guide, transfer code simulations were run with the other nominal conditions. The resulting maximum percent change in TOA radiances ranges from 0.6% to 1.4% for real index variations and from 1.0% to 2.0% for imaginary index variations, with the largest changes occurring for the shorter wavelength bands.

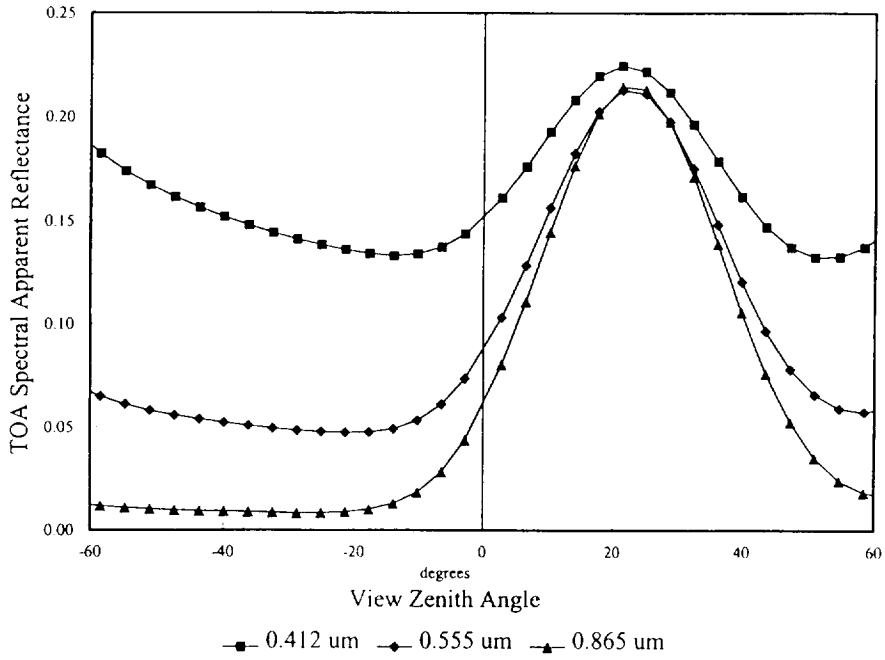

Figure 1. Principal plane slices of the top-of-atmosphere (TOA) apparent reflectance field over Lake Tahoe. Wavelengths correspond to SeaWiFS bands 1, 5, and 8, respectively. Negative view zenith angles imply the antispecular side of nadir.

Large discrepancies also result from uncertainties in aerosol size distribution parameters. The RSG normally employs a Junge size distribution for calibration work. Optical extinction data is fit to a power law to retrieve an associated Ångstrom coefficient.[13] Typical standard deviations in this parameter fit are around 0.5. Using this value as a guide, transfer code simulations were run with the other nominal conditions. The differences range from 3.5% to 7.9%, with the largest changes occurring for the shortest wavelengths. The choice of lower particle size limit, $\alpha_o = 2\pi r_o \lambda^{-1}$, where r_o is the spherical particle radius, also affects the TOA radiances. The exclusion of small particle sizes leads to noticeable signal changes, especially for the shorter visible bands, due to the importance of scattering contributions. Varying this lower limit from $\alpha_o = 0.0001$ to $\alpha_o = 0.001$ changes the TOA radiance between 0.2% and 0.4%. The largest changes occur for the shorter wavelength bands. Finally, the Junge model is only an approximation to the true particle size distribution. A study of the differences resulting between the use of a Junge model compared to the size distribution obtained by inverting spectral optical depths was conducted at WSMR by Hart of the RSG.[13] It was found that errors as large as 3.6% could occur on days for which the Junge distribution clearly does not apply, though values on the order of 0.2% were more common. While not investigated, these errors are expected to be greater over low reflectance targets due to the greater influence of atmospheric scattering.

The high elevation of Lake Tahoe results in low optical depths between site and sensor level. However, to investigate the trends in TOA radiance levels with optical depth, the molecular and aerosol optical depths were varied over a sizeable range. The resulting percent changes in TOA radiances are shown in Figures 2a-b. Increasing the molecular optical depth to its corresponding value at sea level results in an increase in TOA radiance of 11.7% for band 1 and 1.0% for band 8; doubling the aerosol optical depth results in a decrease of 0.4% and 1.0% for these bands, respectively. These studies illustrate the influences of site elevation and aerosol loading. The changes in TOA radiances due to measurement uncertainties for these parameters are much smaller. The origins of these uncertainties have been described elsewhere in the literature.[14] They arise from uncertainties in the calibration of the solar radiometer used to collect extinction data and, in the case of molecular optical depth, from uncertainties in atmospheric pressure measurements. For band 1 the associated TOA radiance changes are 0.03% and 0.01%, respectively, for molecular and aerosol optical depth.

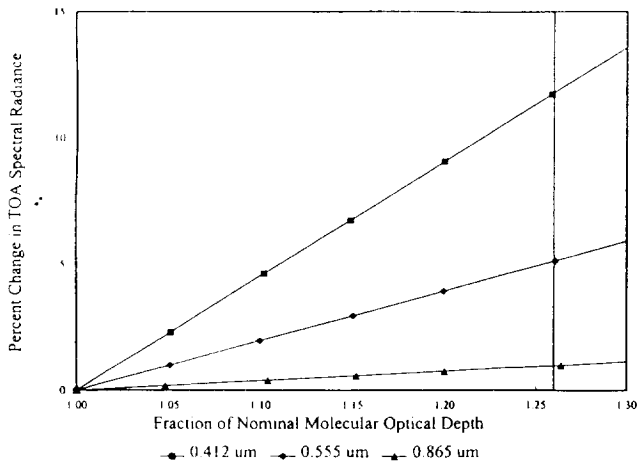

Figure 2a. Percentage change in top-of-atmosphere (TOA) radiance with molecular optical depth. Wavelengths correspond to SeaWiFS bands 1, 5, and 8, respectively. The respective nominal molecular optical depth values are 0.255, 0.075, and 0.013. Sea level corresponds to the vertical line

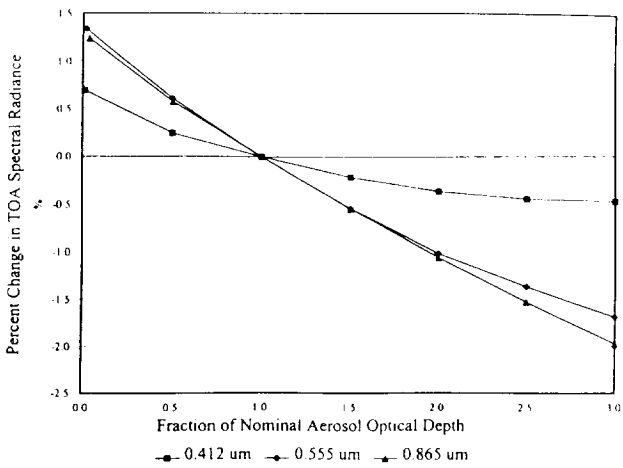

Figure 2b. Percentage change in top-of-atmosphere (TOA) radiance with aerosol optical depth Wavelengths correspond to SeaWiFS bands 1, 5, and 8, respectively. The nominal aerosol optical depths are 0.075, 0.051, and 0.027, respectively

For bright targets, gaseous absorption may be modeled as the direct-to-direct attenuation caused by constituent gases.[11] Over low reflectance targets, absorption effects become more convoluted since the photons received at sensor level are less likely to have traveled along the direct-to-direct path. The changes in TOA radiance due to uncertainties in columnar values assuming this direct-to-direct scheme is valid are highly spectral dependent, but less than 1.0% for all SeaWiFS bands. The discrepancies resulting from the use of this simplified approach were investigated. A radiative transfer code which makes use of a line-by-line absorption band integration scheme coupled with atmospheric scattering[15] was used as a reference for the computation of coupled scatter-absorption features. For a SZA of 40° or less and a wind speed of 5.0 m/s, the discrepancies remain below the 1.5% level for all but band 7, which contains a strong oxygen absorption line. These discrepancies increase with SZA due to the increased atmospheric path length. Within the sun glint region, the discrepancies are negligible for all bands.

Other inputs to the SO transfer code include the vertical distribution of molecules and aerosol particles. The code assumes an exponential decay in the number of both constituents as a function of altitude. This model is well established for the molecules in the atmosphere; an effective model is assumed for the aerosols. Varying the effective scale height over a wide range of values was observed to cause changes less than 0.2% in the TOA radiance for all bands.

The RSG has been able to measure reflectances within an uncertainty of ±0.01 for bright reflectance targets. This same uncertainty level is assumed to hold for lower reflectance targets. For water targets this uncertainty is undoubtedly overestimated - especially at longer wavelengths - since the water-leaving radiance should only be affected by variations in chlorophyll content. Nevertheless, this uncertainty represents the believed current measurement capability of the RSG. Associated changes in TOA radiance vary between 4.7% for band 1 and 12.1% for band 8. The larger changes at longer wavelengths result from the increased importance of the surface contribution. Another source of reflectance uncertainty arises from the precision of wind speed measurements - known to ±0.1 m/s. Associated changes in TOA radiances are less than 0.05% for all bands.

A comparison of the inherent accuracy of SO to other numerical solution techniques was made for high reflectance sites.[16] This comparison showed agreement between SO and the other codes at the 1% level. An analogous comparison has not been conducted for water targets since the codes used for the previous comparison are not able to model such surfaces. Instead, the 1% level of uncertainty has been assumed to hold.

2.3. Calibration uncertainties

Uncertainty estimates have been compiled for each SeaWiFS band using all combinations of solar zenith angle, view zenith angle, and wind speed studied. The complete database of uncertainties is too vast to be presented in its entirety. It is sufficient to discuss the observed trends in these uncertainties under different solar, wind, and

viewing conditions. The changes in TOA radiance are reduced when the viewing geometry lies in the region of sun glint. This is due to the decreased importance of the atmospheric signal contributions. The changes are also reduced for smaller solar zenith angles due to the reduced path through the aerosols. Altering wind speed also has a slight effect on the overall calibration uncertainty - with changes being greatest outside the sun glint region for small wind speeds and long wavelengths.

A representative uncertainty table is presented in Table 2. For this table, a solar zenith angle near 20°, a wind speed of 5.0 m/s, and a near-nadir viewing geometry were chosen. HA is the aerosol vertical distribution scale height, W is the wind speed, T_{gas} is the gaseous transmittance, 'code' is the believed code accuracy, and E_{sun} is the uncertainty in exoatmospheric solar irradiance.

Table 2. TOA radiance uncertainties for the SeaWiFS spectral bands using the reflectance-based method. All values are quoted as one sigma percentages.

Source	Band 1	Band 2	Band 3	Band 4	Band 5	Band 6	Band 7	Band 8
$\delta_{molecular}$	< 0.1	< 0.1	< 0.1	< 0.1	< 0.1	< 0.1	< 0.1	< 0.1
$\delta_{aerosol}$	< 0.1	< 0.1	< 0.1	< 0.1	< 0.1	< 0.1	< 0.1	< 0.1
$n_{aerosol}$	1.3	1.4	1.2	1.2	1.1	0.9	0.8	0.6
$k_{aerosol}$	2.0	2.0	1.9	1.7	1.6	1.3	1.2	1.0
ν	7.9	7.9	7.1	6.5	6.1	4.6	4.4	3.5
HA	0.2	0.2	< 0.1	< 0.1	< 0.1	< 0.1	< 0.1	< 0.1
α_o	0.4	0.4	0.3	0.3	0.3	0.2	0.2	0.2
ρ_{water}	4.7	5.6	6.9	7.6	8.7	11.0	11.7	12.1
W	< 0.1	< 0.1	< 0.1	< 0.1	< 0.1	< 0.1	< 0.1	< 0.1
T_{gas}	< 0.1	< 0.1	0.2	0.5	1.0	0.5	1.7	0.1
code	1.0	1.0	1.0	1.0	1.0	1.0	1.0	1.0
E_{sun}	1.0	1.0	1.0	1.0	1.0	1.0	1.0	1.0
RSS	9.6	10.1	10.3	10.3	11.0	12.1	12.8	12.7

From Table 2, it is obvious that the reflectance-based approach at Lake Tahoe is not a viable stand-alone calibration method. In order for the uncertainties to drop within acceptable levels, significant advancements in the measurement of in-water reflectance and the aerosol size distribution must be made. Such advances can only come through the development of improved instrumentation.

3. RADIANCE-BASED CALIBRATION

The radiance-based method is newer than its reflectance-based counterpart. Sensors calibrated by RSG personnel using this method include SPOT-2 HRV[17] and a helicopter-mounted Daedalus multispectral scanner[18]. It has also been used to calibrate the Nimbus-7 Coastal Zone Color Scanner (CZCS)[19], though data was collected at altitudes much higher than those flown by the RSG. The technique uses aircraft-based measurements of the spectral radiances upwelled from a calibration site at sensor overpass. Optical extinction measurements and meteorological data permit the retrieval of optical depths and gaseous absorption constituents. These parameters are used to transfer the measured radiances through the remaining atmosphere to their TOA values.

3.1. Radiative transfer code

As for the reflectance-based method, the SO code was selected for use with radiance-based calibrations over water targets; the 5S code was again employed to compute gaseous absorption. These codes play a different role in the radiance-based calibration process than in reflectance-based calibrations. For the latter, they are used to compute the entire TOA signal; for the former, they are used only to transfer aircraft-level radiances to sensor level. Code input uncertainties again lead to changes in the TOA radiances but can be expected to be less important, due to the reduced role of the codes. As the size of the correction between aircraft-level and TOA decreases, these uncertainties produce smaller changes in the TOA radiances.

3.2. Transfer of aircraft-level radiances to TOA

Over high reflectance calibration targets, the correction term applied to the aircraft-level signal is a small residual and the exact transfer process is less important than the calibration of the field radiometer. For low reflectance sites, this transfer becomes more critical because a large portion of the TOA signal still comes from the atmosphere remaining above the aircraft. This is especially true for shorter visible wavelength bands. Shown in Figure 3a are profiles of near-nadir spectral radiance as a function of altitude for bands 1, 5, and 8 over Lake Tahoe. Shown in Figure 3b are similar profiles for band 1 with three different viewing geometries: antispecular; near-nadir; and specular. These profiles have been scaled relative to their TOA value and generated using the conditions presented in Table 1 with a SZA near 20° and a wind speed of 5.0 m/s. A typical aircraft altitude flown during radiance-based calibrations, 3.67 km MSL, is included in each figure. Note that the correction is greater for the shorter wavelength bands and for viewing geometries outside the sun glint region due to the relative importance of atmospheric signal, but that this signal arises mostly from well-characterized molecular scatter.

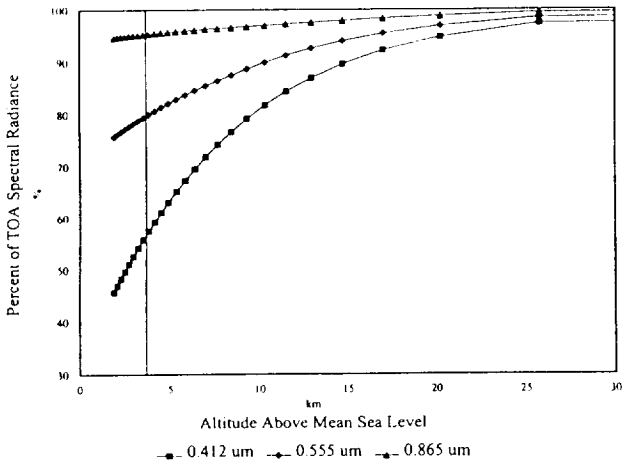

Figure 3a. Altitude profiles of spectral radiance scaled to top-of-atmosphere (TOA) values. Wavelengths correspond to SeaWiFS bands 1, 5, and 8, respectively. The curves are presented for a near-nadir viewing geometry. Lake elevation is 1.9 km. Aircraft level is shown as 3.67 km.

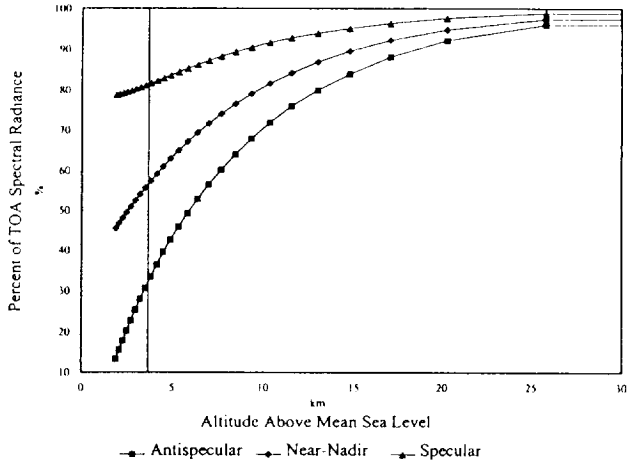

Figure 3b. Altitude profiles of spectral radiance scaled to top-of-atmosphere (TOA) values for three viewing geometries. The curves are presented for a wavelength of 0.412 μm which corresponds to SeaWiFS band 1. Lake elevation is 1.9 km. Aircraft level is shown as 3.67 km.

One approach to transfer the radiance field to sensor level is to assume the field at aircraft-level is isotropic, that is, equal to the measured value for all upward directions. Outside the sun glint direction, this method underestimates the TOA signal. Glint contributions coupled into the viewing direction by the nearly symmetric phase function, which is almost entirely molecular in nature, are neglected by the isotropic boundary assumption. A better approach is to use the radiative transfer code to compute the ratio of the sensor-level signal to that at aircraft level. An absolute value is then determined using the measured aircraft-level value and the remaining gaseous transmittance between aircraft and sensor, which arises primarily from ozone and molecular oxygen. In this way, the angular distribution of the aircraft-level radiance field is not discarded. The resulting transfer relation becomes

$$L_\lambda^{TOA} = L_\lambda^{AC}\left(\frac{\rho_\lambda^{TOA}}{\rho_\lambda^{AC}}\right) T_{gas}^{AC-TOA} \qquad (1)$$

where L_λ^{TOA} is the TOA radiance, L_λ^{AC} is the aircraft-level radiance, ρ_λ^{TOA} is the computed TOA apparent reflectance, ρ_λ^{AC} is the computed aircraft-level apparent reflectance, and $T_{gas}^{AC\text{-}TOA}$ is the gaseous transmittance between aircraft-level and TOA. The sensitivity study for this transfer method is described in the following sections.

3.3. Sensitivity study

The set of permutations described in Section 2.3 was used for the sensitivity study of the radiance-based method. The primary difference between these two studies is that, for the radiance-based method, it is the stability of the TOA radiance field relative to the aircraft-level field that is important rather than the absolute stability of the TOA signal. The absolute calibration of the field radiometer is also important.

An additional source of error for this method is the pointing accuracy of the radiometer. Since the upwelled radiance field exhibits a high degree of angular variation, especially at longer wavelengths, an uncertainty in orientation can lead to significant changes in collected radiance. An equally important problem is the effect of angular field of view. A large field of view may help to stabilize the aircraft-level signal with respect to pointing error at the expense of not matching that of the sensor being calibrated. These effects are extremely dependent on the radiometer, the viewing direction, and the solar and wind conditions present during the calibration.

3.4. Calibration uncertainties

Uncertainty estimates have been compiled for each SeaWiFS band using all combinations of solar zenith angle, view zenith angle, and wind speed studied. As for the reflectance-based method, the changes in TOA radiance are sizably reduced in the region of sun glint. The overall uncertainty is more significantly altered by increases in solar zenith angle than the reflectance-based method, but is more stable for changes in wind speed. A representative uncertainty table is presented in Table 3. For this table, a solar zenith angle near 20°, a wind speed of 5.0 m/s, and a near-nadir viewing geometry were chosen. The category L_λ^{AC} corresponds to the calibration uncertainty of a RSG field radiometer having spectral bands similar to those of SeaWiFS.[20]

Table 3. TOA radiance uncertainties for the SeaWiFS spectral bands using the radiance-based method. All values are quoted as one sigma percentages.

Source	Band 1	Band 2	Band 3	Band 4	Band 5	Band 6	Band 7	Band 8
$\delta_{molecular}$	< 0.1	< 0.1	< 0.1	< 0.1	< 0.1	< 0.1	< 0.1	< 0.1
$\delta_{aerosol}$	< 0.1	< 0.1	< 0.1	< 0.1	< 0.1	< 0.1	< 0.1	< 0.1
$n_{aerosol}$	0.1	0.3	0.4	0.4	0.4	0.4	0.4	0.3
$k_{aerosol}$	0.2	< 0.1	0.2	0.2	0.3	0.3	0.4	0.3
v	1.2	0.2	0.6	0.8	1.1	1.1	1.2	1.0
HA	0.5	0.4	0.3	0.3	0.3	0.2	0.2	0.1
α_o	< 0.1	< 0.1	< 0.1	< 0.1	< 0.1	< 0.1	< 0.1	< 0.1
ρ_{water}	5.0	4.3	3.4	3.3	2.2	1.4	0.9	0.5
W	< 0.1	< 0.1	< 0.1	< 0.1	< 0.1	< 0.1	< 0.1	< 0.1
$T_{gas}^{AC\text{-}TOA}$	< 0.1	< 0.1	0.2	0.4	1.0	0.5	0.7	< 0.1
L_λ^{AC}	0.8	2.1	3.6	2.0	0.8	0.1	1.6	0.6
RSS	5.2	4.8	5.0	4.0	2.8	1.9	2.4	1.4

For this transfer method, the most important parameters again include those related to surface reflectance as well as, for certain bands, the calibration of the field radiometer. Slight changes in surface reflectance dramatically change the radiance field distribution, altering the relationship between aircraft-level and TOA. Note also that the aerosol vertical distribution scale parameter is of greater significance for this method since it affects the reflectance ratio between these two altitudes. To reduce method uncertainties, more precision in the measurement of the Ångstrom coefficient and surface reflectance are required - again implying the need for better instrumentation. In addition, the effects of pointing error and field of view need to be studied.

4. CALIBRATION OF AVIRIS AT LAKE TAHOE

On June 22, 1995 vicarious calibrations of AVIRIS were carried out by the RSG and a group from the University of Southern Florida (USF). Atmospheric measurements were made using a manual, 10-channel solar radiometer and meteorological instruments; diffuse reflectance data were collected from a research vessel using a spectroradiometer designed and built in-house by the USF group; absolute radiance data were collected at an altitude of approximately 3.9 km MSL using a Barnes Modular Multispectral 8-channel Radiometer (MMR)[21]. During the measurement period, the average wind speed was approximately 0.75 m/s and the solar zenith angle progressed from 29° to 25°.

The corresponding reflectance- and radiance-based calibration results are presented in Figure 4 and Table 4. Included for comparison are the results of a laboratory calibration carried out by the Jet Propulsion Laboratory (JPL), along with their quoted uncertainty estimates. Calibration coefficients were generated for the AVIRIS bands that most closely match the first four MMR band centers: 0.49 μm, 0.56 μm, 0.66 μm, and 0.83 μm. These wavelengths roughly correspond to SeaWiFS bands 3, 5, 6, and 8. The radiance-based coefficients were computed using an average of data collected along the AVIRIS flight track in the vicinity of the research vessel. Three passes were made over this area around the time of AVIRIS overpass.

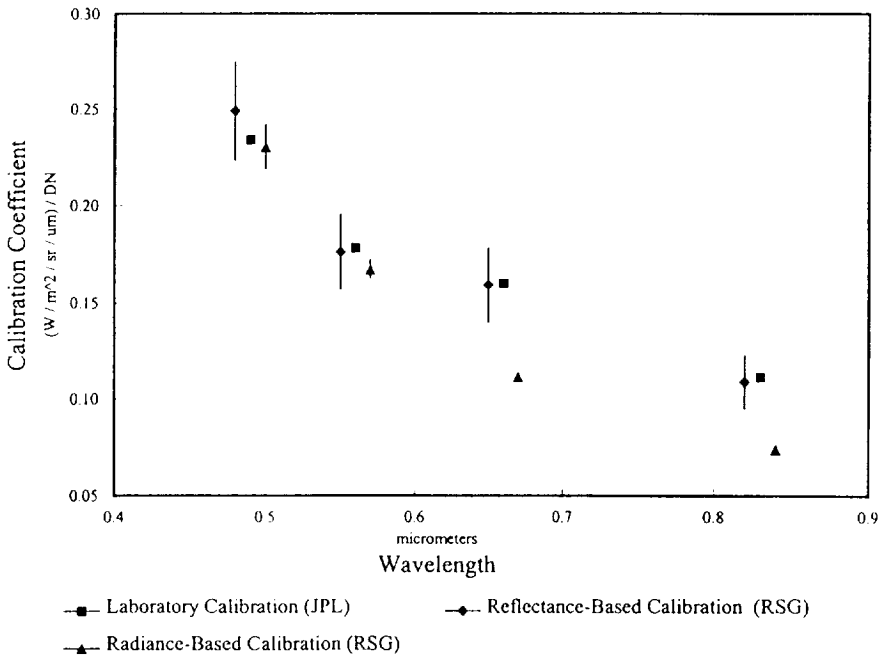

Figure 4. Calibration results for AVIRIS bands 12, 19, 29, and 50. The band centers are 0.49 μm, 0.56 μm, 0.66 μm, and 0.83 μm, respectively. Results from the three methods have been offset to improve clarity.

As is evident in Figure 4, the results of the reflectance-based calibration are in close agreement with the laboratory-based coefficients. The theoretical uncertainties of the reflectance-based method presented in Section 2.3

appear to be slightly overestimated. This is most likely due to the assumed uncertainty for in-water reflectance. It is therefore felt that the method is better than the uncertainty analysis presented in Table 2 indicates. Further refinement of these estimates will be possible after an analysis of collected in-water reflectance data can be made.

The radiance-based method theoretical uncertainties are too small for all but the first band to explain the discrepancies from the JPL coefficients. This was the first attempt made at using the Barnes radiometer as a calibrated instrument. The uncertainties in its calibration are undoubtedly higher than those presented in Table 3. Much work remains to be done in order to properly characterize the instrument. The low signal levels in the longer wavelength bands make linearity of the calibration an important issue. By introducing a pointing error of $\pm 2^{\circ}$ in zenith and azimuth angles into the calibration procedure, radiance changes of 8.6% and 39.0% were observed for band 1 and band 4, respectively. These changes illustrate the importance of reducing pointing uncertainties and properly characterizing the angular response of the radiometer, which has been measured to extend non-negligibly out to $\pm 5^{\circ}$.

Table 4. Results of June 22, 1995 AVIRIS calibrations. Calibration coefficients are quoted in units of ($W\ m^{-2}\ sr^{-1}\ \mu m^{-1}$) / DN for Barnes MMR band centers. Uncertainties are quoted as one sigma percentages.

Method	Band 1 Coefficient (Uncertainty)	Band 2 Coefficient (Uncertainty)	Band 3 Coefficient (Uncertainty)	Band 4 Coefficient (Uncertainty)
Laboratory-based Method (JPL)	0.2344 (1.0)	0.1785 (1.0)	0.1603 (1.0)	0.1113 (1.0)
Reflectance-based Method (RSG)	0.2492 (10.3)	0.1763 (11.0)	0.1593 (12.1)	0.1088 (12.7)
Radiance-based Method (RSG)	0.2307 (5.0)	0.1676 (2.8)	0.1116 (1.9)	0.0739 (1.4)

5. CONCLUSIONS

The present work has shown the viability of using existing vicarious methods to calibrate sensors over low reflectance sites. An analysis of the error sources for the reflectance-based and radiance-based methods has been carried out and presented. The associated uncertainty estimates indicate that there is a need for better precision in the measurement of surface reflectance and aerosol properties. Experimental verification of the two techniques has been attempted using AVIRIS imagery. The results indicate that the reflectance-based technique is more stable than the radiance-based technique at longer wavelengths. The latter is highly dependent on the proper characterization of the field radiometer at low signal levels and the minimization of pointing errors.

6. ACKNOWLEDGMENTS

This work was partially funded by NASA contracts NGT-30239 and NAGW-3543. The authors wish to thank JPL for supplying the needed AVIRIS image and M. Chami for the initial processing of the image. We also gratefully acknowledge C. Curtis from the Department of Physics at the University of Arizona, B. Richards from the Tahoe Research Group of the University of California at Davis, B. Steward from the USF, and the staff of the Truckee-Tahoe airport for their assistance during the AVIRIS calibration data collection period. Finally, we thank P. Dubuisson for his aid in analyzing the effect of decoupling gaseous absorption from atmospheric scattering.

7. REFERENCES

1. Gordon, H.R. (1987), Calibration requirements and methodology for remote sensors viewing the ocean in the visible, *Remote Sens. Environ.* **22**: 103-126.

2. Thome, K.J., Gellman, D.I., Parada, R.J., Biggar, S.F., Slater, P.N., and Moran, M.S. (1993), In-flight radiometric calibration of Landsat-5 Thematic Mapper from 1984 to present, *Proc. SPIE* **1938**(14): 126-130.

3. Gellman, D.I., Biggar, S.F., Dinguirard, M.C., Henry, P.J., Moran, M.S., Thome, K.J., and Slater, P.N. (1993), Review of SPOT-1 and -2 calibrations at White Sands from launch to present, *Proc. SPIE* **1938**(13): 118-125.

4. Gordon, H.R., Brown, O.B., Evans, R.H., and Clark, D.K. (1983), Nimbus 7 CZCS: reduction of its radiometric sensitivity with time, *Appl. Opt.* **22**(24): 3929-3931.

5. Slater, P.N., Biggar, S.F., Holm, R.G., Jackson, R.D., Mao, Y., Moran, M.S., Palmer, J.M., and Yuan, B. (1987), Reflectance- and radiance-based methods for the in-flight absolute calibration of multispectral sensors, *Remote Sens. Environ.***22**: 11-37.

6. Kaufman, Y.J., and Holben, B.N. (1993), Calibration of the AVHRR visible and near-IR bands by atmospheric scattering, ocean glint and desert reflection, *Int. J. Remote Sensing* **14**: 21-52.

7. Hovis, W.A., Clark, D.K., Anderson, F., Austin, R.W., Wilson, W.H., Baker, E.T., Ball, D., Gordon, H.R., Mueller, J.L., El-Sayed, S.Z., Sturm, B., Wrigley, R.C., and Yentsch, C.S. (1980), Nimbus-7 Coastal Zone Color Scanner: system description and initial imagery, *Science* **210**: 60-63.

8. Hooker, S.B., and Firestone, E.R., eds. (1992), *SeaWiFS Technical Suport Series: Volume 1, An overview of SeaWiFS and ocean color*, NASA, Technical Memorandum 104566, Vol. 1, NASA Goddard Space Flight Center, Greenbelt, MD 20771, 25pp.

9. Santer, R., Gu, X.F., Guyot, G., Deuzé, J.L., Devaux, C., Vermote, E., and Verbrugghe, M. (1992), SPOT calibration at the La Crau test site (France), *Remote Sens. Environ.* **41**: 227-237.

10. Deuzé, J.L., Herman, M., and Santer, R. (1989), Fourier series expansion of the transfer equation in the atmosphere-ocean system, *J. Quant. Spectrosc. Radiat. Transfer* **41**: 483-494.

11. Tanré, D., Deroo, C., Duhaut, P., Herman, M., Morcrette, J., Perobos, J., and Deschamps, P.Y. (1987), *Simulation of the Satellite Signal in the Solar Spectrum (5S)*, (revised), Laboratoire d'Optique Atmosphérique, Université des Sciences et Techniques de Lille, 59655 Villeneuve d'Ascq Cedex, France, 264pp.

12. Herman, B.M. (1989), Personal communication to S.F. Biggar, Department of Atmospheric Sciences, University of Arizona.

13. Hart, Q.J. (1991), Surface and aerosol models for use in radiative transfer codes, *Proc. SPIE* **1493**(18): 163-174.

14. Biggar, S.F., Gellman, D.I., and Slater, P.N. (1990), Improved evaluation of optical depth components from Langley plot data, *Remote Sens. Environ.* **32**: 91-101.

15. Dubuisson, P. (1996), Personal communication, Laboratoire de Physique Appliquée au Milieu Océanique Côtier - Station Marine, Université du Littoral, France.

16. Moran, M.S., Jackson, R.D., Slater, P.N., and Teillet, P.M. (1991), Comparison of atmospheric correction procedures for visible and near-IR satellite sensor output, *ESA SP-319.*

17. Biggar, S.F., Slater, P.N., and Gellman, D.I. (1994), Uncertainties in the in-flight calibration of sensors with reference to measured ground sites in the 0.4 to 1.1 μm range, *Remote Sens. Environ.* **48**: 245-252.

18. Balick, L.K., Golanics, C.J., Shines, J.E., Biggar, S.F., and Slater, P.N. (1991), The in-flight calibration of a helicopter-mounted Daedalus multispectral scanner, *Proc. SPIE* **1493**(24): 215-223.

19. Hovis, W.A., Knoll, J.S., and Smith, G.R. (1985), Aircraft measurements for calibration of an orbitting spacecraft sensor, *Appl. Opt.* **24**(3): 407-410.

20. Biggar, S.F. (1996), Personal communication, Optical Sciences Center, University of Arizona.

21. Robinson, B.F., Bauer, M.E., Dewitt, D.P., Silva, L.F., and Vanderbilt, V.C. (1979), Multiband radiometer for field research, *Proc. SPIE* **196**: 8-15.

An improved symmetric gaussian wave-slope model for radiative transfer codes

R. J. Parada

Remote Sensing Group, Optical Sciences Center, University of Arizona,
Tucson, Arizona 85721

ABSTRACT

Atmosphere-ocean radiative transfer problems require the use of a wave-slope distribution model to describe the state of the water surface. An expression for this distribution was derived empirically by Cox and Munk[1]. This expression, which in general depends on both wind speed and direction, is often approximated as being azimuthally (or radially) symmetric to reduce the complexity of transfer code algorithms. The symmetric gaussian model widely employed in transfer codes does not always return acceptable results. The current work presents a symmetric model which more closely matches the non-symmetric model of Cox and Munk. The implementation of the model to realistic modeling situations shows that it has a sizable effect on the results of transfer computations.

1. INTRODUCTION

1.1. Cox and Munk distribution

The purpose of the current work is to find a symmetric wave-slope model which most closely matches the features of the true distribution. The Cox and Munk model[1,2] has been widely accepted by the scientific community as accurately representing reality and is therefore a good reference to which others may be compared. This distribution is nearly radially symmetric and is close to being gaussian in form. In the alongwind direction, the slopes are skewed to a non-zero value due to the asymmetric form of the waves. The waves also contain a degree of peakedness which causes the model to further deviate from a symmetric gaussian form. These eccentricities are accounted for by a Gram-Charlier series. The complete formulation of the model is presented in Equation 1.

$$p(\xi,\eta) = (2\pi\sigma_c\sigma_u)^{-1}\exp\left[-\frac{1}{2}(\xi^2+\eta^2)\right]\left\{1-\frac{1}{2}c_{21}(\xi^2-1)-\frac{1}{6}c_{03}(\eta^3-3\eta)+\frac{1}{24}c_{40}(\xi^4-6\xi^2+3)\right.$$
$$\left.+\frac{1}{4}c_{22}(\xi^2-1)(\eta^2-1)+\frac{1}{24}c_{04}(\eta^4-6\eta^2+3)\right\} \qquad (1)$$

The variables ξ and η are the crosswind and upwind (i.e. alongwind) slope components normalized by the corresponding rms slopes, σ_c and σ_u, respectively. Series coefficients c_{21} and c_{03} give the skewness characteristic of the distribution; coefficients c_{40}, c_{22} and c_{04} give its peakedness. The coefficients and rms slopes were determined by regression of data collected during measurements of sun glitter patterns on the ocean's surface and were found to depend on the wind speed, W, near the ocean surface. The resulting relations (with wind speed given in units of m/s) are presented in Equations 2 and 3.

$$\begin{aligned} c_{21} &= 0.01 - 0.0086W \pm 0.03 \\ c_{03} &= 0.04 - 0.033W \pm 0.12 \\ c_{40} &= 0.40 \pm 0.23 \\ c_{22} &= 0.12 \pm 0.06 \\ c_{04} &= 0.23 \pm 0.41 \end{aligned} \qquad (2)$$

$$\sigma_c^2 = 0.003 + 0.00192W \pm 0.002$$
$$\sigma_u^2 = 0.000 + 0.00316W \pm 0.004 \quad (3)$$

As seen in Equation 3, the crosswind rms slope component contains a factor which is independent of wind speed. This prevents the distribution from approaching radial symmetry at low wind speeds as it should (i.e. since there is essentially no alongwind direction). The model should therefore not be extended into this low-wind regime. Whether or not this constant factor actually exists or is merely an artifact of the data regression is a matter of some debate.[3,4]

1.2. Cox and Munk symmetric gaussian approximation

The complexity of the two-dimensional, non-symmetric Cox and Munk model make it difficult to incorporate into radiative transfer and atmospheric correction algorithms. A simple approximation to this model is made by ignoring the Gram-Charlier series and using an effective rms slope component, σ, which is assumed to be independent of wind direction. The associated form of this distribution is presented in Equation 4.

$$p(z_x, z_y) = (\pi\sigma^2)^{-1} \exp[-(z_x^2 + z_y^2)/\sigma^2] \quad (4)$$

Here, z_x and z_y represent the wave-slope components in orthogonal directions. The effectiveness of this approximation depends on the selection of σ. The most common choice[5-9] is the sum of the crosswind and alongwind rms slope components from the non-symmetric Cox and Munk model, i.e. the rms slope component which is independent of direction,[1,10] as presented in Equation 5.

$$\sigma^2 = \sigma_c^2 + \sigma_u^2 = 0.003 + 0.00512W \quad (5)$$

For very low wind speeds, this choice results in a symmetric model which is only half as broad as the crosswind component of the non-symmetric Cox and Munk model. This leads to an overestimation of small wave-slopes and an underestimation of large ones. As wind speed increases, the associated distribution becomes wider than the non-symmetric model. This leads to a reverse situation in which small wave-slopes are underestimated and large wave-slopes are overestimated. In addition, this choice of σ fails to account for the skewness and peakedness features of the more general, non-symmetric model.

2. DETERMINATION OF AN IMPROVED SYMMETRIC GAUSSIAN MODEL

2.1. Fitting algorithm

An algorithm based on the minimization of sum-squared error (SSE) between the non-symmetric Cox and Munk model (c.f. Equation 1) and a symmetric gaussian model (c.f. Equation 4) was used to determine the value of σ that would provide the best agreement between the two. The use of SSE results in a fit which is insensitive to the sign of errors between the two and weights larger errors much more strongly. For a given wind speed, the range of wave-slopes over which the general Cox and Munk model is assumed valid, $-2.5 \le \xi,\eta \le 2.5$, is subdivided into a set of evenly spaced grid points. The SSE between the two models is computed using the error at each grid point to compute an approximate integral. This is carried out for two closely spaced values of σ so that an approximate derivative, $dSSE/d\sigma$, may be formed. The best-fit value is found by bisecting the interval within which this derivative changes sign - converging, within some tolerance, to the σ at which it becomes zero-valued.

As stated in Section 1.1, the general (non-symmetric) Cox and Munk model is not valid for low wind speeds. As seen in Equation 3, the alongwind rms slope component becomes zero-valued as wind speed reduces to zero. This seems to indicate that in the alongwind direction only zero-valued slopes exist. The wave distribution should actually become nearly symmetric in azimuth since the alongwind direction is undefined. Mathematically, this means that the model should not be applied for wind speeds at which the alongwind rms slope component is less than the crosswind component, i.e. when σ_u is less than σ_c. After equating the relations in Equation 3, the cut-off wind speed

is found to be about 2.4 m/s. For wind speeds below this value, it is necessary to modify the general model using some reasonable assumptions concerning the nature of the true wave-slope distribution for such cases. In the absence of a prevailing wind, the wave-slope distribution is assumed to be radially symmetric. Furthermore, since the crosswind rms slope component contains a factor which is independent of wind speed, only this component should remain in the absence of any wind. It is therefore reasonable to assume that in the low-wind regime all directions have the same rms slope component, and that this component will tend toward σ_c as the wind speed decreases toward zero. Finally, since the skewness of the Cox and Munk model depends on the presence of a prevailing wind direction, it is also reasonable to assume that this feature becomes nonexistent for low-wind conditions - leaving only the peakedness terms of the associated Gram-Charlier series. With these reasonable assumptions in hand, the curve fitting algorithm described above may be employed. For the low-wind regime, the general Cox and Munk model is modified so that both the upwind and crosswind rms components are set to σ_c and the skewness terms are removed. It is worth noting that, should the constant factor in the expression for σ_c^2 be found to not actually exist, this modification of the general Cox and Munk distribution becomes unnecessary since the alongwind rms slope component remains greater than the crosswind component at all finite wind speeds.

2.2. Results of fitting algorithm

The fitting algorithm was used to compute the best-fit value of σ for wind speeds between 0.0 m/s and 20.0 m/s at an interval of 0.1 m/s. For the fitting algorithm, 101 x 101 grid points were used with a convergence tolerance of 1.0×10^{-6} on σ. The raw data are shown in Figure 1. Note that these data have a wind speed dependence which is nearly bilinear in form. The two segments correspond to the low- and sizable-wind regimes.

The integrated absolute error arising due to deviations from the general Cox and Munk model are shown as a function of wind speed in Figure 2 for several choices of σ: the original symmetric model (c.f. Equation 5); a two-dimensional non-symmetric gaussian model formed by truncating the Gram-Charlier series to the first (unity) term; the best-fit data obtained from the fitting algorithm; a symmetric model using the alongwind rms slope component, $\sigma^2 = 2\sigma_u^2$; and a symmetric model using the crosswind rms slope component, $\sigma^2 = 2\sigma_c^2$. This error was computed by integrating the absolute error between a given model and the general Cox and Munk model, modified for the low-wind regime, over the range of valid wave-slopes (c.f. Section 2.1). This error gives an indication of the effectiveness of the model. Since each model itself integrates to unity, models returning an error below 0.01 may be considered an effective substitute for the general Cox and Munk distribution at a given wind speed. Overall, the best-fit σ^2 data out-performs the other models. Its integrated error remains below 0.01 for wind speeds above 5.2 m/s, and never rises above 0.02 over the entire range of studied wind speeds. The original symmetric model climbs above 0.01 at a wind speed of 11.5 m/s and increases dramatically below 1.5 m/s due to the decreasing width of the distribution. A similar increase in error at low wind speeds is observed from the use of the alongwind rms slope component for this same reason. It is interesting to note that the truncated Cox and Munk model, which retains its non-symmetric nature while ignoring the skewness and peakedness features, performs worse than the best-fit data - indicating that these eccentricities have an important impact on the gaussian fitting process. This truncated model converges to the error resulting from the use of the crosswind rms slope component at low wind speeds since it is modified in this regime similar to the general Cox and Munk distribution so that $\sigma_u \rightarrow \sigma_c$.

The crosswind and alongwind slices of several wave-slope distributions are shown in Figures 3a-b for a wind speed of 5.0 m/s. From these figures, it is clear that the best-fit data is a better fit to the general Cox and Munk model than both the original symmetric and the truncated non-symmetric gaussians.

2.3. Regression of the best-fit data

Relations between the best-fit data and wind speed have been determined using two regressions. The first is a simple linear fit; the second is a bilinear fit which splits the studied wind speeds into two regions. The general form used to derive the relationship linking σ^2 and wind speed is presented in Equation 6.

$$\sigma^2 = a_0 + a_1 W \tag{6}$$

The linear model was derived from a linear regression of the best-fit data over the entire range of studied wind speeds. For the bilinear model, this range was subdivided into two regions: the low-wind regime which includes

wind speeds below a value of 2.4 m/s; and the sizable-wind regime which includes all higher wind speeds. These regions were both fitted using linear regressions of the best-fit data. A summary of the regression results for these two models is presented in Table 1.

Table 1. Summary of regression results for linear and bilinear symmetric gaussian models.

Regression Parameter	Linear Model	Bilinear Model Low-wind Regime	Bilinear Model Sizable-wind Regime
Constant, a_0	0.003594	0.005515	0.003035
Std Err of Y Estimate	4.2×10^{-4}	2.3×10^{-7}	2.5×10^{-5}
Linear Coefficient, a_1	0.004557	0.003530	0.004598
Std Err of Coefficient	5.1×10^{-6}	6.3×10^{-8}	3.7×10^{-7}
No. Of Observations	201	25	176
Degrees of Freedom	199	23	174
R-Squared	0.999751	1.000000	0.999999

The percent error of each fit is shown as a function of wind speed in Figure 1. The bilinear model agrees at better than the 0.1% level for wind speeds in the sizable-wind regime; this error drops to the 0.01% level in the low-wind regime. The linear fit provides a poorer fit which worsens at low wind speeds - resulting in a fit error near 30% at 0.1 m/s. Based on these results, the bilinear fit is believed to provide the best model for the fitting routine results.

3. RADIATIVE TRANSFER CODE SIMULATIONS

3.1. Selection and description of radiative transfer model and expected results

The radiative transfer code selected to test the new wave-slope models was the Successive Orders[9] (SO) program developed by the Laboratoire d'Optique Atmosphérique at the University of Lille, France. In this code, the transfer equation for the upwelled radiance field is numerically solved for an atmosphere composed of molecules and spherical particles. This transfer equation is decomposed as a function of azimuth into a Fourier series. An associated transfer equation is solved for each of a set of fixed view zenith angles (VZAs). The model divides a plane-parallel, horizontally-homogeneous atmosphere into 26 layers of equal optical depth. Successive orders of scattering are introduced until the resulting radiance field converges or until the maximum scattering order is reached. The direct-to-direct (i.e. sun glint) component of the radiance field is then added. This contribution is not included in the Fourier series expansion because it is highly directional and would require a very large number of expansion terms - increasing the computation time unnecessarily.

One benefit arising from this numerical scheme is that the glint component is computationally isolated from the other radiance contributions. Therefore, its effects on the radiance field may be readily observed. The corresponding radiance relation is presented in Equation 7. In this equation, $\{L^n\}$ represent the Fourier series components of the diffuse radiance field computed by the transfer code up to convergence order N; $\{\delta_{0,n}\}$ are Kroneker delta functions; L_G represents the unattenuated glint component of radiance; and τ represents the total optical depth. The angles θ_s and θ_v are the solar and view zenith angles, respectively while ϕ represents the relative azimuth angle between solar and viewing directions. The spectral dependence of the radiance field, while not explicitly written, is implied.

$$L(\theta_v,\theta_s,\phi) = \sum_{n=0}^{N} (2-\delta_{0,n}) L^n(\theta_v,\theta_s)\cos(n\phi) + L_G(\theta_v,\theta_s,\phi)\exp\left[-\tau\left(\frac{1}{\mu_v}+\frac{1}{\mu_s}\right)\right] \quad (7)$$

In the sun glint region (i.e. the *specular* viewing direction), the final term on the right hand side of Equation 7 dominates and a nearly linear relationship with the glint signal exists. By further expanding this glint signal, its relationship to the wave-slope distribution may be directly observed, as seen in Equation 8. In this equation, L_{dir} is the direct solar radiance which has not been attenuated by the downward optical extinction. $R(\Theta)$ represents the Fresnel reflectance coefficient of a wave facet which contributes a glint contribution in the viewing direction, with angle Θ bisecting the angle between the solar and view directions. The wave facet tilt, θ_f, is jointly dependent on the view and solar zenith angles. It is now clear that in the region of sun glint, any changes in the wave-slope distribution will lead to nearly linear changes in the observed radiance.

$$L_G(\theta_v,\theta_s,\phi) = L_{dir}(\theta_s,\phi_s)\, R(\Theta)\, p(\theta_f,\phi)\, d\theta_f d\phi \tag{8}$$

Away from the sun glint region, the effects of altering the wave-slope distribution will be convoluted by the amount of optical extinction induced by the atmosphere. At shorter visible wavelengths there is a sizable radiance contribution due to molecular atmospheric scatter. Radiance variations due to changes in the surface state (i.e. wave-slope distribution) are less important at these wavelengths. For longer wavelengths, the atmospheric radiance contributions are much less pronounced so that changes in the surface conditions may have sizable effects.

3.2. Test Cases

Conditions corresponding to Lake Tahoe, Nevada were selected for use in comparing the wave-slope models. This is a deep, high-elevation lake containing clear, oligotrophic water. It has been selected as a calibration target for ocean color sensors such as the Sea Viewing Wide Field-of-view Sensor (SeaWiFS)[11] and the Ocean Color and Temperature Sensor (OCTS)[12]. It therefore represents an important case study for the modeling of the radiance field over a water body. A summary of the environmental conditions for this location is given in Table 2. In this table, $n_{aerosol}$ is the real part of the aerosol refractive index, $k_{aerosol}$ is the imaginary part of the aerosol refractive index, $\tau_{aerosol}$ is the aerosol optical depth, $\tau_{Rayleigh}$ is the Rayleigh optical depth, ω_o is the single-scatter albedo, α is the aerosol Ångstrom turbidity coefficient, and ρ_{water} is the effective diffuse reflectance of the water body.

Table 2. A summary of nominal environmental conditions for Lake Tahoe.

Wavelength (μm)	$n_{aerosol}$	$k_{aerosol}$	$\tau_{aerosol}$	$\tau_{Rayleigh}$	ω_o	α	ρ_{water}
0.412	1.44	-0.005	0.0796	0.255	0.859	1.08	0.018
0.865	1.44	-0.005	0.0273	0.013	0.859	1.08	0.000

Two wavelengths were selected for the study: 0.412 μm and 0.865 μm. These wavelengths correspond to the central wavelengths of SeaWiFS[12] bands 1 and 8, respectively, and encompass the spectral range covered by most ocean color sensors. Two representative solar zenith angles were chosen: approximately 20° and 60°. These values represent a typical range of solar zenith angles between summer and winter at Lake Tahoe near local noon. This set of parameters leads to four distinct case studies. Wind speeds between 0.0 m/s and 20.0 m/s were employed for each case. The two models summarized in Table 1 were used, as well as the original symmetric gaussian model described by Equation 5.

3.3. Modeling Results

The top-of-atmosphere (TOA) radiance fields resulting for the four case studies have been plotted in Figures 4a-d for a wind speed of 5.0 m/s. These figures contain principal plane slices of the radiance field specified in terms of apparent reflectance, ρ^*. The relation between ρ^* and radiance, L, is shown in Equation 9. In this equation, μ_s represents the cosine of the solar zenith angle, E_{os} represents the normally incident

exoatmospheric irradiance at the mean earth-sun distance, and d represents the precise earth-sun distance in units of AU. Both ρ^* and L are spectral and directional quantities.

$$\rho^* = \frac{\pi L d^2}{\mu_s E_{os}} \tag{9}$$

For the plots in Figure 4 there is, in general, a pronounced difference between the original and new symmetric models in the sun glint region. For observations in the specular direction, the associated errors as a function of wind speed are shown in Figures 5a-d, using the new bilinear model as a reference. The discrepancy between this model and the others tends to rise as wind speed is decreased, though it diminishes and then changes sign near the point at which the modified Cox and Munk model was used as a reference for the fitting algorithm. In the sizable-wind regime, the use of the original model results in errors between 2-6% and 8-9% for the shorter and longer wavelengths, respectively. The values are slightly higher for larger solar zenith angles. As wind speed is reduced to 0.0 m/s, the discrepancies increase to between 68-75% at 0.412 μm and to near 83% at 0.865 μm. Differences caused by the use of the new linear model remain less than 2-3% in the sizable-wind regime, but increase dramatically as wind speed is decreased to zero.

Outside the sun glint region, the discrepancy between the original and new symmetric gaussian models drops significantly in many cases. The error for observations in the antispecular (i.e. backscatter) direction is shown as a function of wind speed in Figures 6a-d, using the new bilinear model as a reference. The discrepancies of the original model become small as wind speed is reduced. This result indicates that the original model is adequate for certain solar-view geometries as wind speed approaches 0.0 m/s. For the smaller solar zenith angle, the discrepancies at 0.865 μm are significant in the presence of sizable winds - demonstrating that for certain cases, due to the low signal levels present, changes in wave-slope model may have significant effects on the radiance field outside the central region of sun glint. In all cases, the discrepancies observed between the linear model and the bilinear models were seen to be small.

4. CONCLUSIONS AND RECOMMENDATIONS

Two new azimuthally symmetric gaussian wave-slope models have been derived using a fitting algorithm which minimizes the SSE from the non-symmetric Cox and Munk distribution. Comparisons of these models with the commonly employed symmetric distribution have been made. These comparisons show that the computed radiances in the sun glint region are significantly affected by the use of different models. At very low wind speeds, the discrepancies become more substantial. Outside of the sun glint region, differences may become large for certain situations (e.g. for long wavelength, small solar zenith angle, and moderate wind speed).

Based on the findings of the current study, it is advised that the commonly used symmetric gaussian model described by Equations 4 and 5 not be employed in radiative transfer algorithms. For applications requiring a symmetric gaussian distribution, the new bilinear model developed herein is recommended.

As more applications involving the use of oceans and sun glint are developed, such as their use in the calibration of airborne and orbiting sensors,[11-14] the ability to accurately model the radiance upwelled from water surfaces will become increasingly important. New experimental studies of the wave-slope distribution at low wind speeds are needed to determine whether or not the crosswind rms slope component truly contains a factor independent of wind speed. This will permit the refinement of the symmetric models developed herein. As a final note, it is felt that some room for improvement in the development of symmetric wave-slope models still exists. The inherent peakedness of the general Cox and Munk model may be better compensated for by leaving behind the restriction of using a purely gaussian distribution and introducing certain terms of the Gram-Charlier function back into the fitting process.

5. ACKNOWLEDGEMENTS

This work was funded under NASA contracts NGT-30239 and NAGW-3543. R.P. Santer of the Laboratoire de Physique Appliquée au Milieu Océanique Côtier at the Université du Littoral and J.L. Deuzé of the Laboratoire d'Optique Atmosphérique at the University of Lille are gratefully acknowledged for their assistance with the operation and modification of the Successive Orders radiative transfer code. Gratitude is also given to P.N. Slater, K.J. Thome, and S.F. Biggar of the Remote Sensing Group at the Optical Sciences Center of the University of Arizona for creating the impetus for this work.

6. REFERENCES

1. Cox, C.S., and Munk, W.H. (1954), Measurements of the roughness of the sea surface from photographs of the sun's glitter, *JOSA* **44**(11): 838-850.

2. Cox, C.S., and Munk, W.H. (1954), Statistics of the sea surface derived from sun glitter, *Journal of Marine Research* **13**: 198-277.

3. Duntley, S.Q. (1954), Measurement of the distribution of water wave slopes, *JOSA* **44**(7): 574-575.

4. Shaw, J. (1996), Personal communication, Optical Sciences Center, University of Arizona.

5. Voillier, M., Tanré D., and Deschamps, P.Y. (1980), An algorithm for remote sensing of water color from space, *Boundary Layer Meteorology* **18**: 247-267.

6. McClain, C.R., and Yeh, E. (1994), Sun glint flag sensitivity study, *SeaWiFS Technical Support Series: Volume 13, Case Studies for SeaWiFS Calibration and Validation, Part 1*, NASA Technical Memorandum 104566, Vol. 13, NASA Goddard Space Flight Center, Greenbelt, MD 20071, pp.46-47.

7. Vermote, E., Tanré, D., Deuzé, J.L., Herman, M., and Morcrette, J.J. (1995), *Second Simulation of the Satellite Signal in the Solar Spectrum (6S)*, Laboratoire d'Optique Atmosphérique, Université des Sciences et Techniques de Lille, 59655 Villeneuve d'Ascq Cedex, France, 211pp.

8. Gordon, H.R. (1994), Modeling and simulating radiative transfer in the ocean, *Ocean Optics*, Spinrad, R.W., Carder, K.L., and Perry, M.J. eds., Oxford Press, New York, pp. 3-39.

9. Deuzé, J.L., Herman, M., and Santer, R. (1989): Fourier series expansion of the transfer equation in the atmosphere-ocean system, *J. Quant. Spectrosc. Radiat. Transfer* **41**: 483-494.

10. Cox, C.S., and Munk, W.H. (1955), Some problems in optical oceanography, *Journal of Marine Research* **14**: 63-78.

11. Parada, R.J., Thome, K.J., and Santer, R.P. (1996), Results of dark target vicarious calibration using Lake Tahoe, *Proc. SPIE* (In press).

12. Shimada, M. (1996), Personal communication, Meeting of the Committee on Earth Observation Satellites Working Group on Cal/Val: Sub-group on Infrared and Visible Optical Sensors, Toulouse, France.

13. Kaufman, Y.J., and Holben, B.N. (1993), Calibration of the AVHRR visible and near-IR bands by atmospheric scattering, ocean glint and desert reflection, *Int. J. Remote Sensing*, **14**: 21-52.

14. Vermote, E., Santer, R.P., Deschamps, P.Y., and Herman, M. (1992), In-flight calibration of large field of view sensors at short wavelengths using Rayleigh scattering, *Int. J. Remote Sensing* **13**(18): 3409-3429.

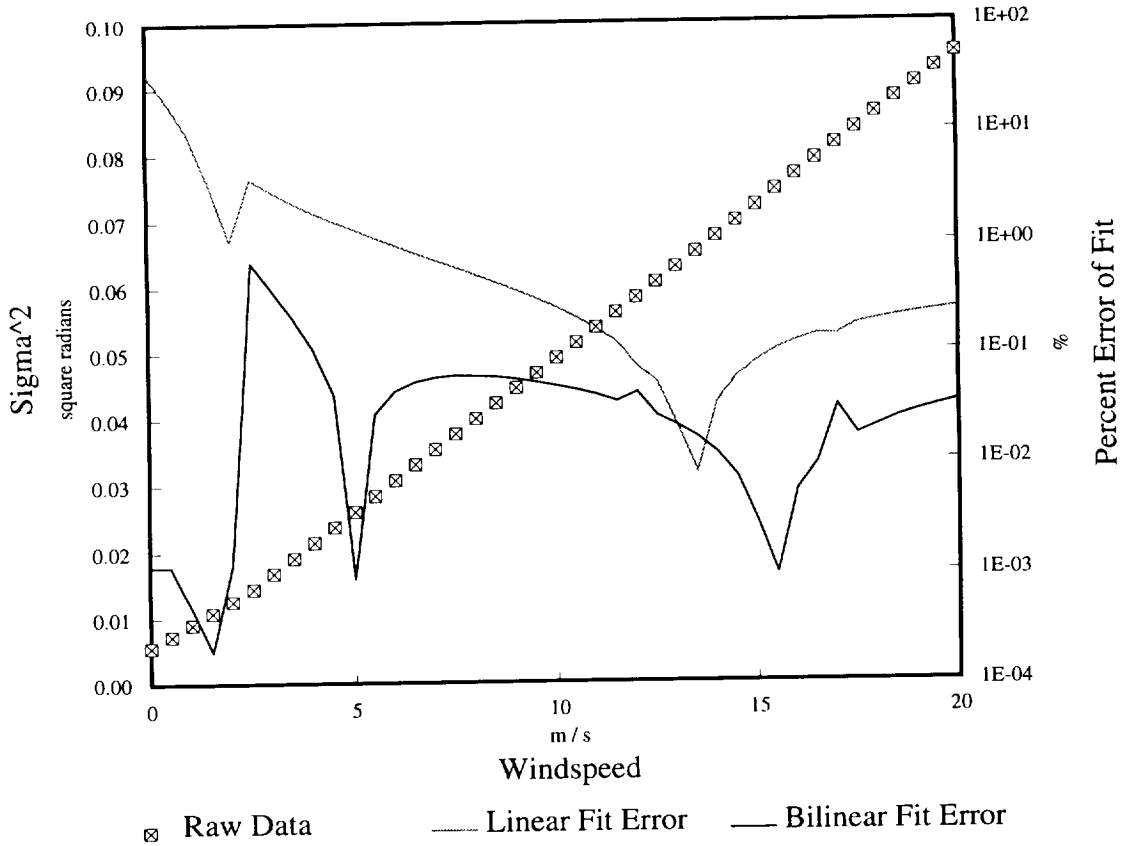

Figure 1. The best-fit rms slope component data for a symmetric gaussian distribution as a function of wind speed. Data points are shown at intervals of 0.5 m/s. The data are very nearly bilinear, with the demarcation near a wind speed of 2.4 m/sec. Percent error for linear and bilinear fits to the data are also shown.

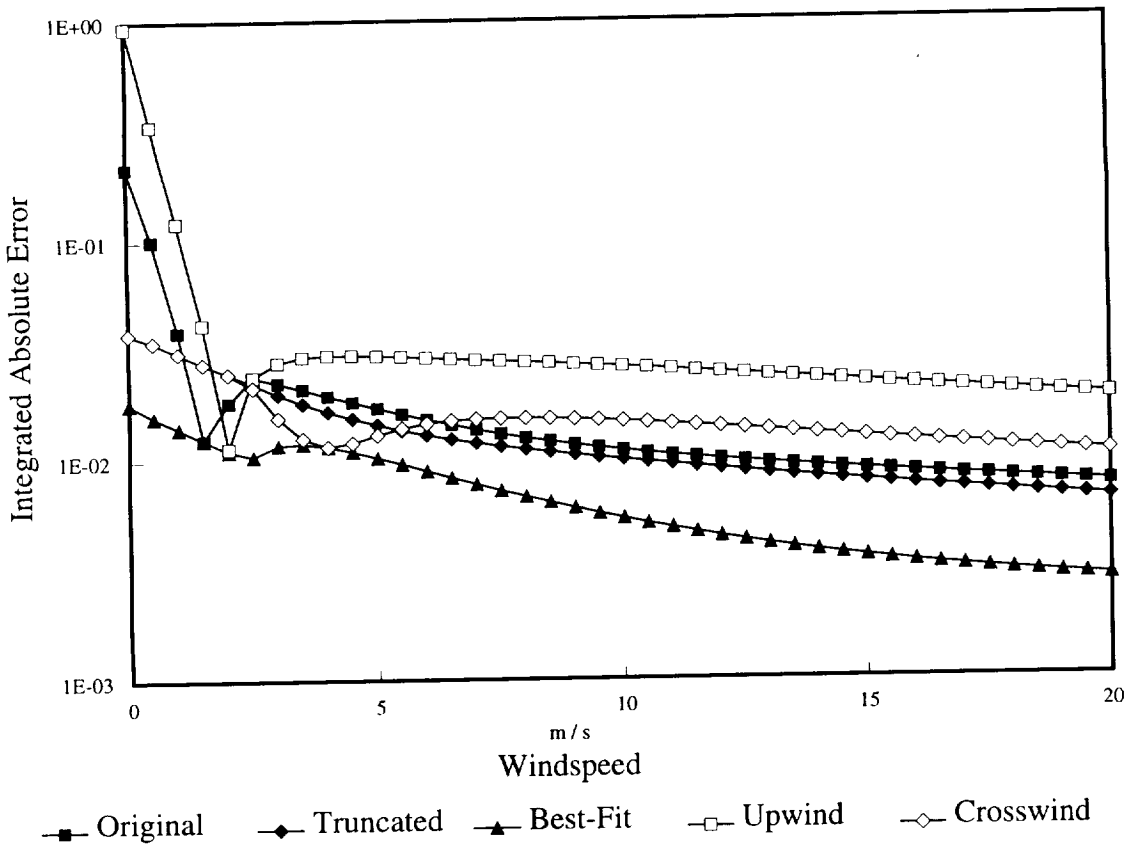

Figure 2. The integrated absolute error between several simpler models and the general, non-symmetric Cox and Munk distribution (modified for low wind speeds). Data points are shown at intervals of 0.5 m/s. The error is integrated over the range of validity in wave-slope space for the Cox and Munk model at a given wind speed.

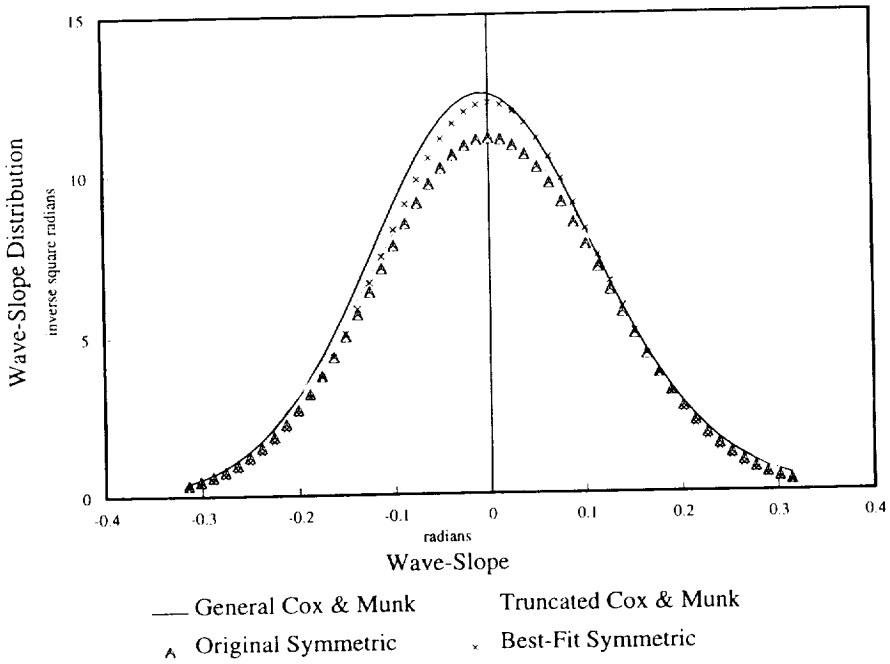

(a) Alongwind slice

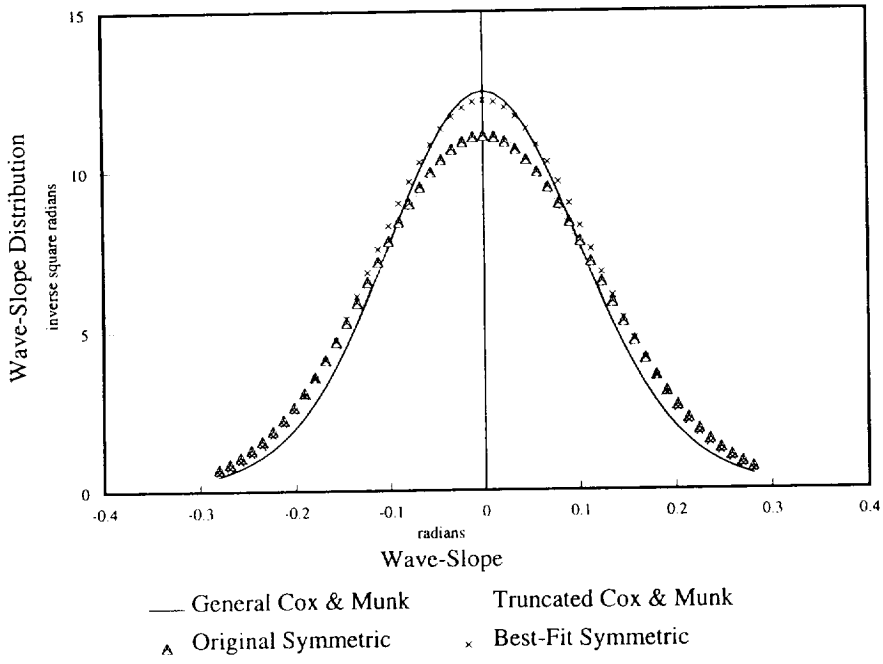

(b) Crosswind slice

Figure 3. Alongwind and crosswind slices through various wave-slope distributions for a wind speed of 5.0 m/s.

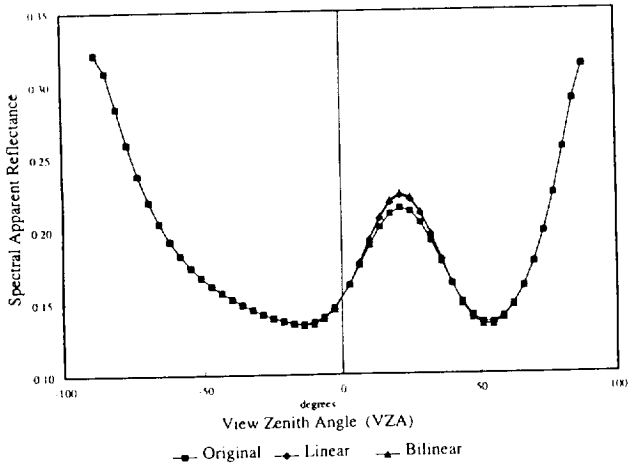

(a) Case 1: Wavelength = 0.412 μm Solar Zenith Angle = 20°

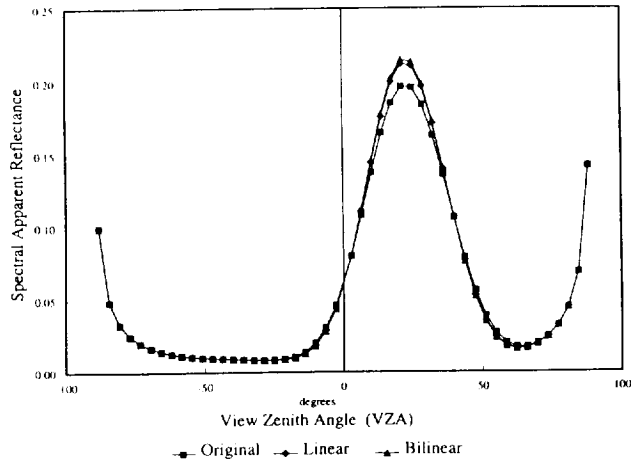

(b) Case 2: Wavelength = 0.865 μm Solar Zenith Angle = 20°

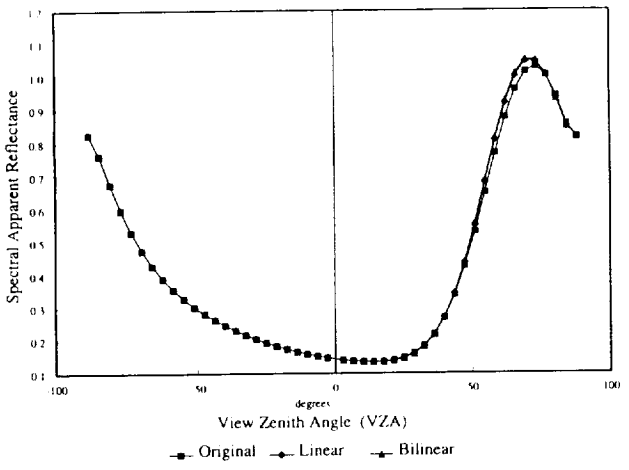

(c) Case 3: Wavelength = 0.412 μm Solar Zenith Angle = 60°

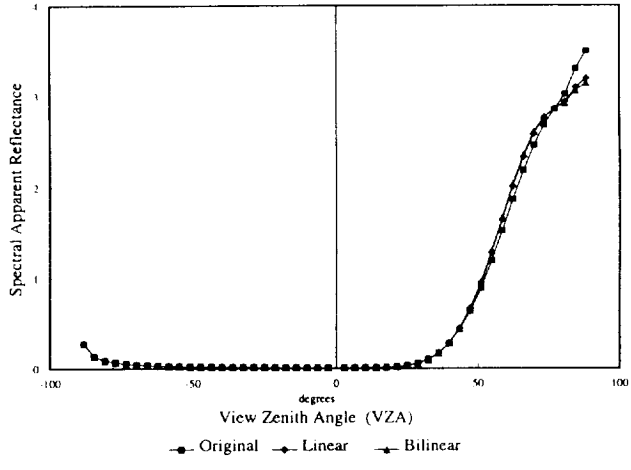

(d) Case 4: Wavelength = 0.865 μm Solar Zenith Angle = 60°

Figure 4. Principal plane slices through the top-of-atmosphere radiance field computed using various wave-slope models at a wind speed of 5.0 m/s. Negative view zenith angles imply the antispecular side of nadir.

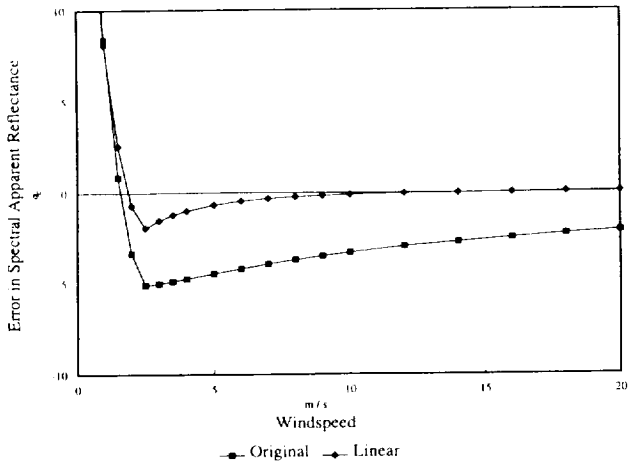

(a) Case 1: Wavelength = 0.412 μm Solar Zenith Angle = 20°

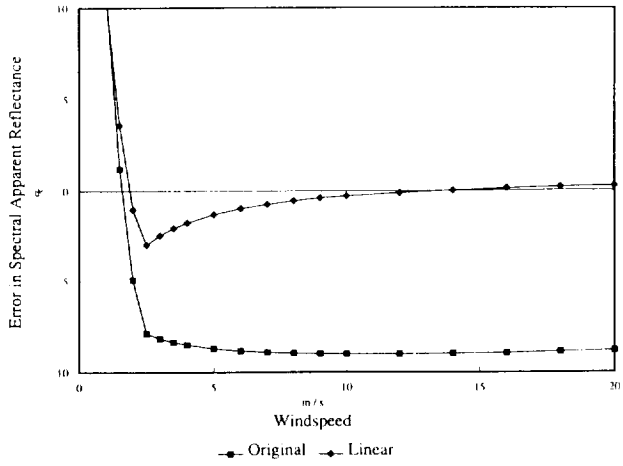

(b) Case 2: Wavelength = 0.865 μm Solar Zenith Angle = 20°

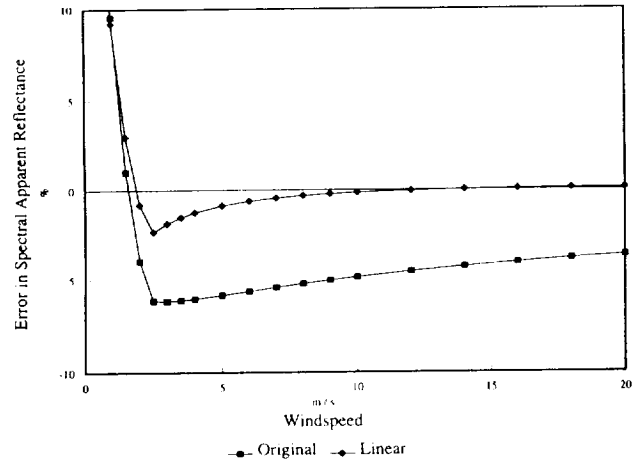

(c) Case 3: Wavelength = 0.412 μm Solar Zenith Angle = 60°

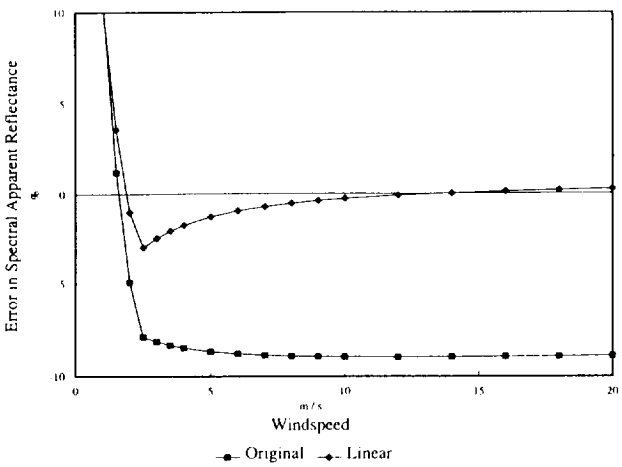

(d) Case 4: Wavelength = 0.865 μm Solar Zenith Angle = 60°

Figure 5. A comparison of peak sun glint radiances computed using various wave-slope models as a function of wind speed. The new bilinear distribution was used as the reference for error computation.

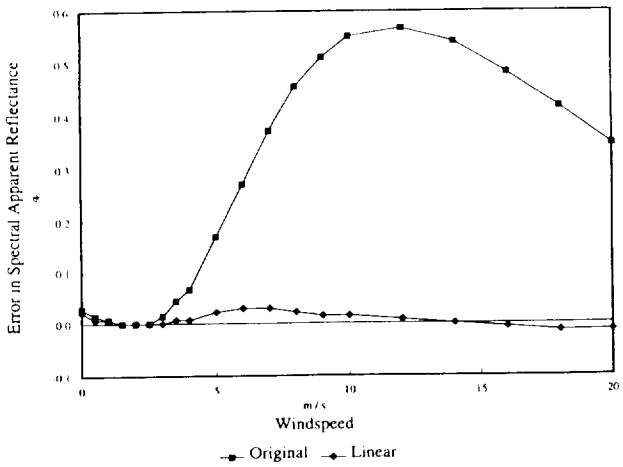

(a) Case 1: Wavelength = 0.412 μm Solar Zenith Angle = 20°

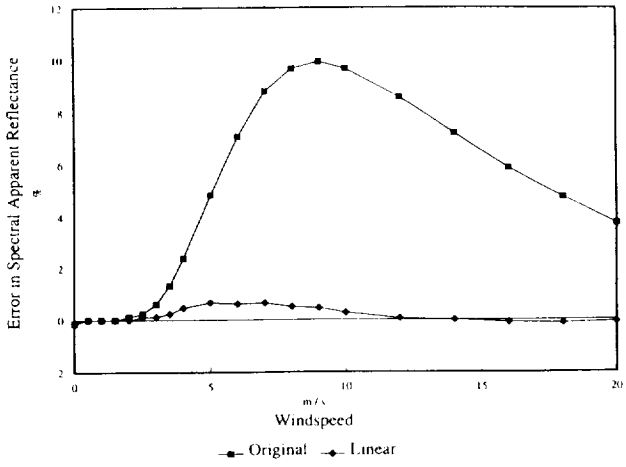

(b) Case 2: Wavelength = 0.865 μm Solar Zenith Angle = 20°

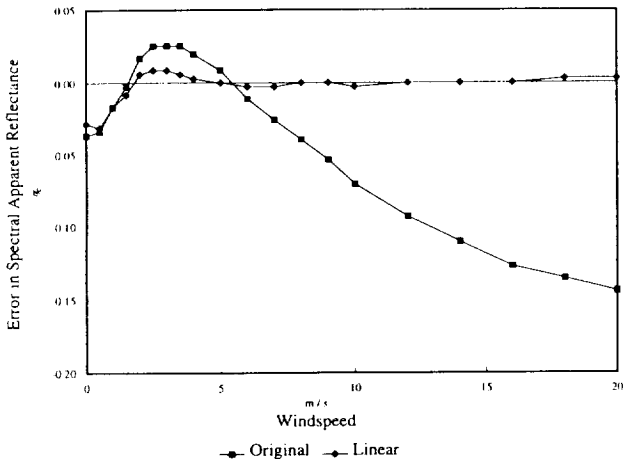

(c) Case 3: Wavelength = 0.412 μm Solar Zenith Angle = 60°

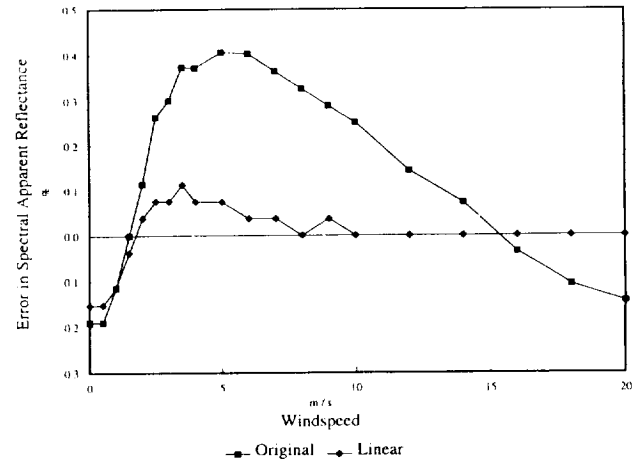

(d) Case 4: Wavelength = 0.865 μm Solar Zenith Angle = 60°

Figure 6. A comparison of antispecular (i.e. backscatter) radiances computed using various wave-slope models as a function of wind speed. The new bilinear distribution was used as the reference for error computation.